applied optics

# Optical fiber couplers for precision spaceborne metrology

Christian J. Killow,[1,*] Ewan D. Fitzsimons,[1,2] Michael Perreur-Lloyd,[1] David I. Robertson,[1] Henry Ward,[1] and Johanna Bogenstahl[3]

[1]Scottish Universities Physics Alliance (SUPA), School of Physics and Astronomy, Institute for Gravitational Research, University of Glasgow, Glasgow G12 8QQ, UK
[2]UK Astronomy Technology Centre, Royal Observatory Edinburgh, Edinburgh EH9 3HJ, UK
[3]Max Planck Institute for Gravitational Physics, Albert Einstein Institute, Callinstraß e 38, D-30167 Hannover, Germany
*Corresponding author: Christian.Killow@glasgow.ac.uk

Received 17 December 2015; revised 23 February 2016; accepted 28 February 2016; posted 29 February 2016 (Doc. ID 256048); published 30 March 2016

**We describe the optical and mechanical design, construction philosophy, and testing of a pair of matched, space-flight-qualified fiber couplers. The couplers were developed for the LISA Pathfinder mission but are relevant for other applications—both on ground and in space—where a robust fiber coupler with well-controlled beam parameters and stable beam pointing is required. This particular implementation of the design called for two couplers providing collimated beams with individual waist sizes and positions. The target values were a 522 μm waist 145 mm after the collimating lens for one coupler and a virtual 520 μm waist 194 mm before the collimating lens for the second coupler. Values of (542 ± 4) μm at (142 ± 19) mm and (500 ± 8) μm at (−275 ± 8) mm were achieved, fully meeting the mission requirements. To control spurious noise effects in the interferometer, the optical system design also specified tight limits on relative beam curvature at an intended interference point. With nominal curvatures at this location of ∼2.35 m, the matching between the outputs of the two fiber couplers was measured to be $\lambda/33$ peak–valley over the central 1 mm of the beams. Results showing pointing stability of 3 μrad/°C over a 50°C range are presented. The vibration, shock, and thermal vacuum environmental testing conditions to which a pair of qualification fiber couplers were subjected—without change in performance—are listed.** 

***OCIS codes:*** (120.6085) Space instrumentation; (060.2310) Fiber optics.

http://dx.doi.org/10.1364/AO.55.002724

## 1. INTRODUCTION

The LISA Pathfinder mission [1] is a technology demonstrator for a spaceborne gravitational wave observatory, such as the proposed eLISA [2–4]. LISA Pathfinder consists of two inertially free test masses, shielded from external forces. The test masses are surrounded by electrode systems that can capacitively sense and electrostatically control their positions and attitudes. Closed-loop control of the spacecraft position with respect to the masses is achieved by ejecting nitrogen from cold gas thrusters to generate micro-Newton forces. The primary goal of the mission is to demonstrate the quality of relative inertial free-fall of the two masses. The critical measurement that probes this behavior is a very-low-noise interferometric readout of the relative displacements of the two masses along a single axis.

The Optical Bench Interferometer (OBI) [5] is the hardware that provides the interferometric sensing of test mass positions and orientations. To achieve the mission goals, the relative positions and angles of the test masses must be monitored to better than 10 pm/$\sqrt{\text{Hz}}$ and 20 nrad/$\sqrt{\text{Hz}}$ in the 1–30 mHz frequency range. Under the demanding conditions associated with launch and space operation, excellent dimensional stability of the OBI is required, together with drift-free alignment of optical components. For LISA Pathfinder, this is achieved by assembling the ultrastable OBI using hydroxide catalysis bonding of the fused silica optical components to a Zerodur low-expansion baseplate.

The LISA Pathfinder OBI uses a heterodyne readout and thus requires two frequencies of light. These are generated by the output beam from a single laser—a 1064 nm nonplanar ring oscillator—being split and sent through two acousto-optic modulators with drive frequencies ∼kHz apart. The two frequencies of light are delivered from the modulators to the OBI by single-mode, polarization-maintaining optical fibers.

The fiber end has a large numerical aperture, and the emitted light requires collimation to allow the formation of

interferometers with path lengths of many tens of centimeters. The mode at the exit of the fiber, distance to the collimating lens, and properties of the lens all define the beam that will be produced. The trade-off for an optical layout such as that for LISA Pathfinder is to have a small beam radius to allow small optical components and hence a compact design, while having a large enough Rayleigh range to allow matching of beam sizes and curvatures for interfering beams that have traveled different distances. The requirement for good matching of the beams at the points of recombination is vital in order to produce the good interferometric contrast necessary for a low-noise readout.

The LISA Pathfinder fiber couplers have requirements on beam quality and collimation, and on alignment accuracy and stability, which must be met and maintained over a range of environmental conditions from manufacture and integration, through testing, launch, and on orbit. A study of commercial-off-the-shelf, modified commercial, and custom-built fiber couplers was undertaken which highlighted the challenges associated with achieving and maintaining beam pointing at the required levels. It was decided to develop a new design of fiber coupler that benefited from the constructional techniques—precision alignment and subsequent joining of components using hydroxide catalysis bonding [6,7]—used elsewhere in the OBI build [8].

## 2. CONSTRUCTION AND ALIGNMENT PHILOSOPHY

As well as fulfilling demanding requirements on wavefront quality and collimation, the optical beam from the coupler must also meet stringent position and pointing requirements with respect to the substrate to which it is finally attached. The philosophy adopted was to deal separately with these two main design drivers: first, an optical subassembly would be constructed that produced a suitable beam; and second, this subassembly would be aligned and stably attached to the OBI. This strategy lowered overall risk and allowed for selection of fiber couplers based on completed optical characterization of the as-built couplers.

CAD drawings and a photograph of the fiber coupler design are shown in Fig. 1 with a list of the parts as labeled in Fig. 1(a) in Table 1. These part numbers are referred to throughout this section and are placed in chevrons.

Heraeus Suprasil 1 was used for the majority of the fiber coupler parts due to its low coefficient of thermal expansion, its suitability for shaping and polishing in a variety of geometries, and also its suitability for hydroxide catalysis bonding. EpoTek 301-2 epoxy was used to join parts where the composite structure would need to be worked and polished. Hysol EA9361 epoxy was used for the remaining structural joints not requiring hydroxide catalysis bonding.

The coupler can be considered as three separate optical parts all mounted to a common baseplate: the mounted fiber, the lens assembly, and the polarizer. The construction of these will now be described in turn.

### A. Mounted Fiber

The fiber ⟨4⟩ used was a special procurement based on the single-mode polarization-maintaining Fujikura SM98-PS-U40A fiber. This fiber has a nominal output mode radius of 3.3 ± 0.5 μm but due to the non-Gaussian nature of light emitted from a fiber, measurements of the $1/e^2$ beam intensity values in the far-field closely match those of a virtual Gaussian waist of radius 4 μm, and this value was used during calculations. The fiber was supplied with a protective PEEK sheath ⟨1⟩. The fiber is free within the sheath and was terminated at one end with a commercial AVIM fiber connector by Diamond SA [9].

The first stage of the assembly procedure was to mechanically strip back the PEEK and the polyimide coating on the fiber. The underlying glass fiber was then glued using EpoTek 301-2 into a close-fitting quartz ferrule ⟨5⟩ which was in turn glued into the mounting block ⟨6⟩. The ferrule was used to provide a precise mechanical interface between the fiber and the mounting block, while the mounting block provides a mechanical reference to which the fiber polarization axis was aligned at this stage. The mounting block was a Suprasil cube of side 10 mm with a precision hole drilled to provide good fiber alignment with respect to the cube surfaces.

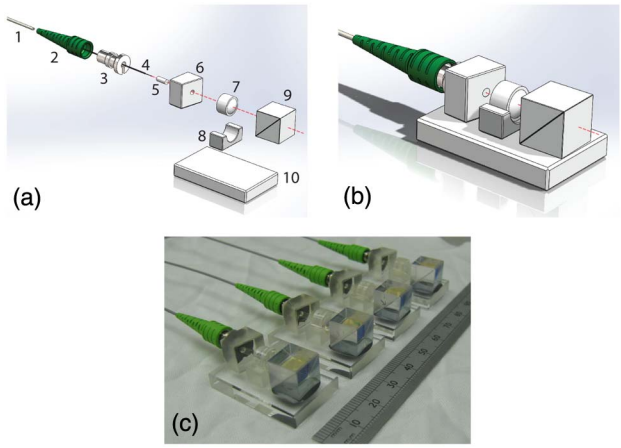


**Fig. 1.** (a) Expanded CAD drawing of the parts of a fiber coupler with the optic axis is shown as a red dashed line, (b) CAD drawing of the assembled fiber coupler with the optic axis shown as a red dashed line, and (c) photograph of four hydroxide catalysis bonded fiber couplers.

**Table 1. Fiber Coupler Parts as Labeled in Fig. 1(a)**

| | |
|---|---|
| Fiber Mounting Parts | |
| 1 | PEEK protective sheath |
| 2 | Hytrel boot to limit fiber bend radius |
| 3 | Titanium strain relief |
| 4 | Optical fiber with partially stripped jacket |
| 5 | Quartz ferrule |
| 6 | Mounting block |
| Lens Assembly | |
| 7 | Aspheric lens |
| 8 | Lens carrier U-groove |
| Polarization Control | |
| 9 | Polarizing beam splitter |
| Baseplate | |
| 10 | Fiber coupler baseplate |

**Table 2. Nominal Lens Parameters**

| | | |
|---|---|---|
| Glass thickness at optic axis (mm) | | 5.358 |
| Refractive index at 1064 nm | | 1.592 |
| | Input surface | Output surface |
| Radius of curvature (mm) | −14.45 | 4.33 |
| Conic constant | −105.23 | −0.8469 |
| 4th-order aspheric constant | $-1.0594 \times 10^{-3}$ | $0.52151 \times 10^{-3}$ |
| 6th-order aspheric constant | $76.926 \times 10^{-6}$ | $-6.8766 \times 10^{-6}$ |

The titanium strain relief part ⟨3⟩ was then glued to the surface of the fused silica block opposite the optical surface and to the protective PEEK sheath. Hysol EA9361 was used for this purpose as it has some compliance when cured which helps to avoid stress concentrations developing in the material due to the difference in coefficients of thermal expansion of the glass and metal.

A rubber boot ⟨2⟩, supplied by Diamond SA, which had previously been slid over the PEEK tubing, was then located on the titanium strain relief part to limit the bend radius at the fiber immediately before the coupler.

The block with the embedded fiber was then polished at an angle of 8° with respect to the optical axis. This was to prevent Fresnel-reflected light from the fiber interface being transmitted back down the fiber and toward the laser and to provide a flat fiber end to ensure good transmitted beam parameters. The mounted fiber was polished, the transmitted beam tested, and the mounting block hydroxide catalysis bonded to the fiber coupler baseplate ⟨10⟩.

A commercial aspheric collimating lens made of ECO-550 (LightPath Technologies part number 352110 ⟨7⟩) was selected following a series of modeling and experimental tests. The nominal lens parameters are listed in Table 2. The cylindrical-shaped lens body was glued into a fused silica "U-groove" mounting piece ⟨8⟩. The U-groove had its base surface polished for hydroxide catalysis bonding and was designed to provide good alignment of the lens optic axis to the light transmitted from the mounted fiber end when both were bonded to the baseplate.

The lens assembly was hydroxide catalysis bonded to the baseplate, as shown in Fig. 2, while controlling the relative spacing of fiber end to lens to ensure that the desired beam parameters were obtained. This was achieved by measuring the transmitted intensity profile at several locations while adjusting the spacing with control at the few micrometer level. The alignment techniques described in [8] were used to achieve this level of position control.

### B. Polarizer

The polarization axis of the light transmitted from the fiber coupler is cleaned by the inclusion of a 1000:1 extinction ratio polarizing beam splitter ⟨9⟩, which was placed after the collimating lens. To reduce power loss to acceptable levels, the slow axis of the fiber was aligned to within 2° of the polarizing beam splitter axis during assembly of the mounted fiber. The beam splitter was glued at an angle of 2° to the beam axis to prevent backreflections propagating through the optical fiber. The polarizing beam splitter was a custom part supplied by CVI Laser Ltd, part number PBS-1064-040-UV. The prisms were made of Corning 7980-1D fused silica and joined using a <15 μm layer of Norland Optical Adhesive 61. The parallelism of input and output surfaces was not highly specified; rather, a batch of components was tested and suitably square components selected.

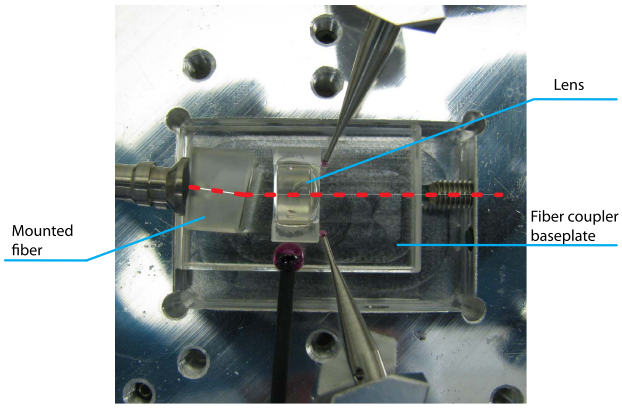


**Fig. 2.** Photograph of a lens assembly being precision-bonded with respect to a mounted fiber onto a fiber coupler baseplate. The red dashed line indicates the beam path. The ruby balls on styli that can be seen entering from the top and bottom are used to control the lens position. The beam profile is monitored to the right of the picture.

### C. Integration with an Optical System

For LISA Pathfinder, each complete fiber coupler subassembly was then precision-bonded to the Zerodur optical bench. The output beam vector was set during bonding using a calibrated target, as described in [10].

Before final adoption for the LISA Pathfinder optical bench, a pair of qualification model fiber couplers underwent successful mechanical and optical testing. The assembly processes used for these test models were then used in the manufacture of the flight hardware.

Comprehensive optical testing and beam pointing stability investigations were performed on the flight hardware couplers; these tests are described in Section 3. The environmental testing performed on the qualification couplers and the flight and flight spare couplers is reported in Section 4.

## 3. OPTICAL DESIGN AND MEASUREMENTS

The requirements on the fiber couplers for the particular case of LISA Pathfinder were derived from the higher-level interferometry requirements of the optical bench interferometer in which beams from two independent fiber couplers are interfered with a path length difference of ∼360 mm. The relevant parameters for quality of interference attributable to the fiber couplers are polarization mismatch, beam size and wavefront matching, and beam pointing stability. The angular and positional alignment of the two beams is not considered here as it is not a property of the couplers. However, the couplers were designed to allow for precision alignment with respect to an optical assembly, as described in [5], where the couplers were aligned to provide

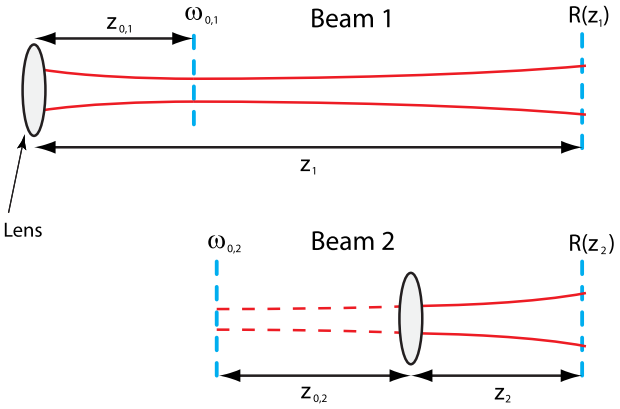


**Fig. 3.** Illustration of beam waist positions for a matched pair of fiber couplers. The laser intensity profile is shown as solid red lines and as dashed red lines for the virtual beam. The intended interference planes are at $R(z)$.

output beams within 30 μrad of the nominally required beam vectors.

Optical modeling was performed using ZEMAX during the coupler design, starting with a 4 μm beam waist to represent the beam at the exit of a fiber. This beam was propagated through a known distance in free space followed by the lens parameters. This resulted in theoretical $1/e^2$ beam intensity values at distances after the lens. The distance between the fiber end and lens was varied to produce two sufficiently collimated beams that were also well matched in size and curvature at the relevant interference points. A sketch of the waist positions is shown in Fig. 3. Each beam has a waist, $\omega_0$, at a distance $z_0$ from the lens. The fiber end (not shown) to lens spacings have been set to optimize the matching of beam sizes and curvatures, $R$, after a propagation distance $z$ where the beams will be interfered. The distance $z$ for each beam is different due to different propagation paths around the optical bench.

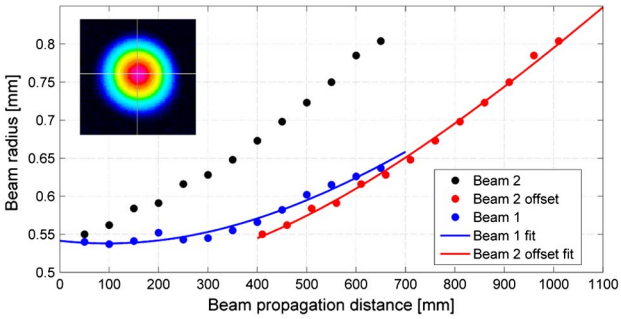


**Fig. 4.** Intensity profiles of propagating beams from a pair of fiber couplers. The solid circles are measured data points, and the lines are fitted profiles. The propagation distances are measured from the coupler outputs, and beam 2 data is also replotted with a 360 mm offset. This demonstrates the satisfactory matching of beam radii at the intended interference locations, which all occur between approximately 400 and 700 mm. Inset: "beam 1" 2D intensity profile at 600 mm.

Nominal distances between the fiber end and lens for the two couplers of 3.40 mm for beam 1 and 3.38 mm for beam 2 were chosen. This modeling was initially verified experimentally by varying the position of a representative lens with respect to a fiber end and then measuring the resultant beam parameters. This gave confidence in the modeling and based on this the qualification and flight pairs of couplers were made. Measured data from the matched flight pair of fiber couplers is shown in Fig. 4, and the modeled and measured data is presented in Table 3. Note that the measured $\omega_0$ and $z_0$ values are those returned from the fitted lines shown in the plot, where Gaussian beam profiles were assumed.

It was not feasible to physically determine the optical path length between the fiber end and the lens surface, so ZEMAX was used to compute the theoretical distance for the measured values of $\omega_0$ and $z_0$ from the fitted profiles. This was calculated to be 3.413 mm and 3.392 mm, a difference of 21 μm compared to the nominal theoretical 20 μm from the initial modeling.

Similar beam profile measurements were made using the qualification pair of fiber couplers at temperatures from 0 to 40°C in 10°C steps. No change in the beam size greater than the 3% measurement error was seen over the whole temperature range.

A Thorlabs WFS150 Shack–Hartmann camera was used to measure the wavefronts of the beams from the flight couplers. The wavefronts were measured at an intended interference plane—~50 cm from the lens for beam 1 and ~15 cm for beam 2—with the results plotted in Fig. 5. The wavefront curvatures were obtained from the data and used to compare the target and achieved values for the individual couplers and to generate a predicted wavefront mismatch of the combined beams.

**Table 3. Modeled and Measured Beam Parameters for a Matched Pair of Fiber Couplers[a]**

| | $\omega_0$ [μm] | $z_0$ [mm] | $Z$ [mm] | $R(z)$ [m] | Peak–Valley | RMS |
|---|---|---|---|---|---|---|
| Beam 1 target | 522 | 145 | 500 | −2.328 | $\lambda/19.8$ | |
| Beam 2 target | 520 | −194 | 150 | −2.384 | $\lambda/20.3$ | |
| Beam 1 result | 542 ± 4 | 142 ± 19 | | −2.635 | $\lambda/22.4$ | $\lambda/46$ |
| Beam 2 result | 500 ± 8 | −275 ± 8 | | −1.792 | $\lambda/15.3$ | $\lambda/35$ |
| | | | Beam 1 wavefront curvature error | | $\lambda/170$ | |
| | | | Beam 2 wavefront curvature error | | $\lambda/61$ | |
| | | | Predicted wavefront mismatch | | $\lambda/45$ | |
| | | | Measured wavefront mismatch | | $\lambda/33$ | $\lambda/200$ |

[a]Intensity beam sizes are $1/e^2$ radii values, and the wavefront values are taken over the central 1 mm. The "wavefront curvature error" is the difference between the target and the result. The parameters described are depicted in Fig. 3. For the peak–valley and RMS measurements $\lambda = 1064$ nm is used.

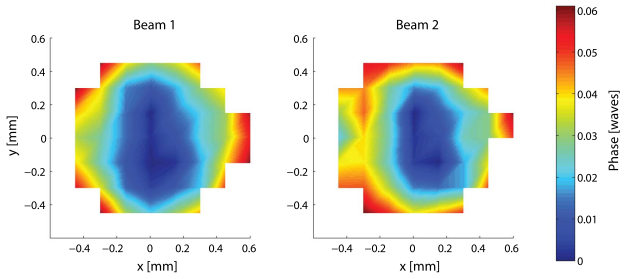


**Fig. 5.** Wavefront profiles of the two fiber couplers over the central 1 mm diameter measured using a Shack–Hartmann sensor. Beam tip/tilt has been removed, and the images have been processed using the interpolative shading function in MATLAB.

The difference between the wavefronts of the two beams, when well aligned and again having traveled the relevant distances, was measured using the spatial phase difference measuring system described in [11]. A custom MATLAB script was used to fit a Gaussian profile to the corresponding intensity data to allow a clip to be centered on the wavefront data, which is plotted in Fig. 6. From this, the peak–valley value was computed that can be compared with the predicted wavefront mismatch from the Shack–Hartmann sensor data.

The modeled and both types of measured data are shown in Table 3. The root mean square for the measured wavefront data is also provided.

The beam radii presented have been the values where the intensity falls to $1/e^2$ from the peak, but the methods for measuring wavefront error do not allow for data at this distance from the beam center. The clips applied to the wavefront data presented are at 1 mm diameter for beams with $1/e^2$ intensity of ~1.6 mm. From [12] we know that an ideal Gaussian beam of radius $\omega$ passing through an aperture of radius $a$ has a normalized transmitted power of

$$P = 1 - e^{-\left(\frac{2a^2}{\omega^2}\right)}. \quad (1)$$

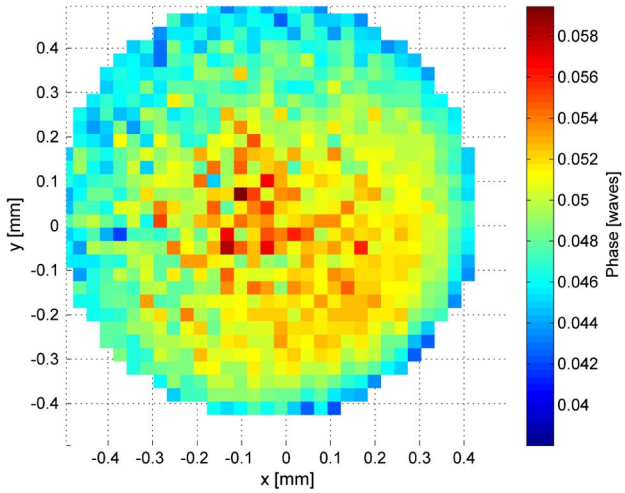


**Fig. 6.** Wavefront difference plot of the combined beams from the two couplers measured using the system described in [11].

Thus, the wavefront error analyses presented are considering 0.79 of the normalized power in the intensity measurements.

The predicted wavefront mismatch at the interference plane —of $\lambda/45$—is entirely due to the difference in curvature. Factors such as imperfections in the lens shape, any imperfection in the beam profile from the fiber, and wavefront error from beam-steering optics in the path to the detectors all contribute to distortion of wavefront shape from nominal, leading to the observed value of $\lambda/33$.

Other optical parameters achieved are beam roundness of >95% and throughput of light from the output of a feed fiber to the output of the fiber coupler of >80%. The end result of the matching of the two fiber couplers was that contrast values in excess of 95% were measured when beams 1 and 2 were combined with the design path length difference.

## 4. ENVIRONMENTAL TESTING

Prior to the assembly of the LISA Pathfinder fiber couplers destined for flight, a pair of couplers was produced for qualification tests, using the same processes described above. These couplers underwent rigorous environmental testing to ensure the manufacturing processes used for the flight pair would result in devices that would survive launch into space and operate within requirements during the mission. There are many other considerations that are generic to producing spaceflight hardware of this nature, such as fracture control analysis and contamination control, but these are omitted here in order to focus on the novel aspects of the work.

### A. Radiation Testing of Component Parts

The transmissive optical components of the couplers, fiber, lens, and polarizing beam splitter were tested to ensure that any darkening due to exposure to radiation in space would not reduce their performance. Sample components were irradiated at the European Space Research and Technology Centre (ESTEC), Netherlands, using a $^{60}$Co $\gamma$-source. These consisted of three lenses irradiated to 20 krad, two to 100 krad, and two beam splitters to 20 krad. The fibers were tested to 20 krad before being supplied, with no observable effects.

Fused silica is known to be radiation hard, but the complexity of obtaining the required aspheric figure and surface finish meant that this material was not considered practicable for the lenses at a reasonable cost and production timescale. In contrast, ECO-550 can be molded to form lenses and suitable lenses for this application were available off-the-shelf. ECO-550 is known to be potentially susceptible to radiation damage, so radiation testing was mandatory. The qualification radiation dose for the LISA Pathfinder optical bench was 20 krad, but the lens material underwent a higher radiation dosage testing in an effort to make the design also relevant to other space missions. The polarizing beam splitters were fused silica with dielectric coatings and Norland Optical Adhesive 61 joining the two halves and as such were not expected to be radiation sensitive at this level.

Optical transmission of the lenses and polarizing beam splitters was measured before and after irradiation using two techniques: an absolute power measurement at 1064 nm and using a Perkin Elmer Lambda 900 spectrophotometer. These results

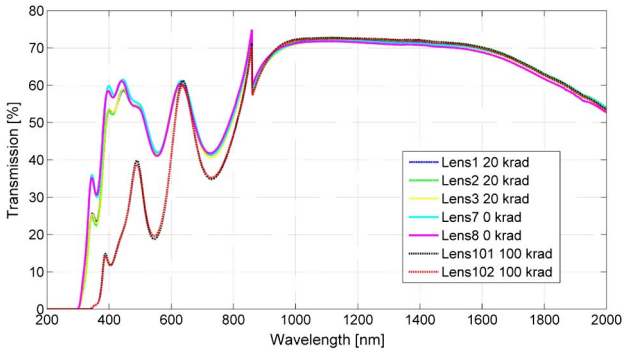


**Fig. 7.** Plot showing relative transmission of both irradiated and nonirradiated collimating lenses as measured by the spectrophotometer. The measurements were made at zero angle of incidence with unpolarized light. Data were taken in nanometer steps and have been averaged over three measurements.

were compared to equivalent results from nonirradiated components. No changes were seen in transmission at 1064 nm within a measurement uncertainty of 0.5%, although the 100 krad irradiated lenses showed darkening at shorter wavelengths, as shown in Fig. 7.

### B. Thermal Vacuum Testing

The fiber couplers underwent a thermal cycling test in air of 20 cycles between 15°C and 40°C over a period of three days with no measureable change in the beam parameters.

Once integrated onto the LISA Pathfinder optical bench interferometer, the fiber couplers were thermal vacuum tested, as described in [5]. At this level of integration, the fiber couplers were hydroxide catalysis bonded to the side of a fused silica post that was bonded to a Zerodur substrate. Also bonded to this substrate were beam-steering mirrors and beam splitters. The optical bench was instrumented with quadrant photodiodes centered on the beams such that beam position could be read out. The photodiodes were at different distances along the beams, allowing—in principle—for the effects of beam angular and lateral motion to be disentangled. In practice, however, mechanisms such as thermal propagation times and hysteresis result in a complex system that is difficult to fully model.

The quadrant photodiode mounts are primarily made of grade 2 titanium with a coefficient of thermal expansion (CTE) of $8.6 \times 10^{-6}$/°C. The fiber coupler is primarily made of fused silica with a CTE of $0.54 \times 10^{-6}$/°C. The beam height above the Zerodur is 12.4 mm, so for a temperature variation of 50°C we can expect a lateral beam movement on the photodiode of ~5 μm peak-to-peak. This will be in the direction perpendicular to the Zerodur bench (out-of-plane).

Figures 8 and 9 show angular beam pointing data from the two fiber couplers as the temperature is varied. The angle was obtained by assuming all motion at the quadrant photodiode was due to changes in the beam angle, with the distances from the fiber coupler to photodiode being 180 mm for beam 1 and 203 mm for beam 2. The movement of the photodiode due to expansion of the titanium mount with temperature was added to the out-of-plane values. The starting beam angle has not been preserved as this is solely dictated by initial alignment.

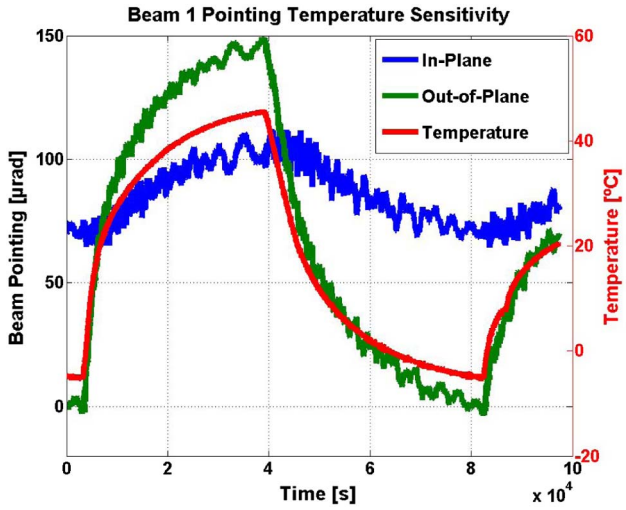


**Fig. 8.** Plots showing variation in beam pointing angle with temperature for beam 1.

The vacuum level when this data was taken was ~10 Pa and the temperature was varied between −5°C and 45°C. The largest effect was seen out-of-plane and was of order 3 μrad/°C, and the effect in-plane was of order 1 μrad/°C.

Such an angular beam variation was expected due to the relatively large CTE of the lens material of $11.6 \times 10^{-6}$/°C, compared to $0.54 \times 10^{-6}$/°C for fused silica. This difference results in a temperature-driven deformation of the lens U-groove assembly. A finite element structural model of the lens in the U-groove was constructed to estimate the effect of temperature changes on the system. The result is shown in Fig. 10. Note that the U-groove is rigidly constrained across the bottom surface and the glue layer is not included in the model so no sliding or separation between the lens and mount is allowed.

In the model, the lens center moves vertically by ~2.3 μm which would result in an angular beam change of around 6 μrad/°C, which is of a similar magnitude to the observed

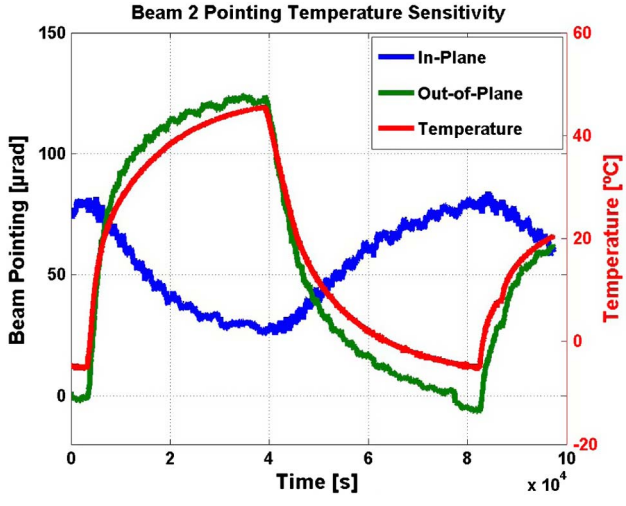


**Fig. 9.** Plots showing variation in beam pointing angle with temperature for beam 2.

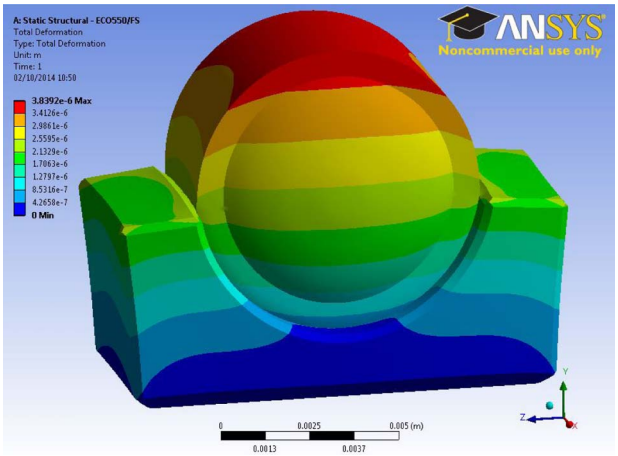


**Fig. 10.** Screen shot showing the finite element analysis of a Lightpath ECO-550 lens mounted in fused silica U-groove for a 40°C temperature change.

values. The difference between modeled and experimental results is likely to be due to the effects of the unmodeled glue layer between the lens and the U-groove, and this could also account for the small variation seen between individual fiber couplers.

The beam motion induced by temperature changes is at a level that would be unmeasurable in most optical systems. Nevertheless, future work will include the development of fiber couplers that are less thermally sensitive for applications with extreme beam pointing stability requirements.

### C. Vibration and Shock Testing

The qualification fiber couplers were subject to vibration and shock testing at the SELEX ES facility in Edinburgh, UK. The Zerodur baseplate to which the couplers were hydroxide catalysis bonded was secured to a hollowed-out aluminum interface plate using quartz wax from Logitech Ltd. The interface plate was bolted directly to the vibration table for $z$ orientation testing and to a slip table attached to the vibration table for $x$ and $y$ orientation testing. In these tests, the $x$–$y$ plane corresponds to "in-plane" and $z$ to "out-of-plane." Table 4 shows the intended test levels.

The sinusoidal and random tests were conducted as per the requirements with a tolerance of 10% on the target acceleration values. The shock levels experienced were within a 6 dB tolerance range apart from above 4 kHz in $x$ and $z$ where it was just below this limit and a slight over-testing below 250 Hz. No change in performance was seen with a measurement uncertainty better than 10 μrad.

The flight and flight-spare pairs of fiber couplers also underwent vibration testing but at acceptance levels. Sine vibration levels were set at 80% of the qualification levels with a sweep rate of four octaves per minute. The acceptance random test levels were -3 dB of qualification and with the duration halved to 60 s. This equated to a total random test load of ~6.3 g RMS in the $x$ and $y$ axes and 7.86 g RMS in the $z$ axis.

**Table 4. Environmental Testing Requirements**

| Sinusoidal Vibration Test Levels (Two Octaves Per Minute Sweep Rate) | | | | | |
|---|---|---|---|---|---|
| x values | | y values | | z values | |
| Frequency (Hz) | Target | Frequency (Hz) | Target | Frequency (Hz) | Target |
| 5 | 8 mm 0-pk | 5 | 9.3 mm 0-pk | 5 | 13.6 mm 0-pk |
| 20 | 13 g | 20 | 15 g | 20 | 22 g |
| 70 | 13 g | 40 | 15 g | 60 | 22 g |
| 90 | 18 g | 60 | 20 g | 80 | 27 g |
| 100 | 18 g | 100 | 20 g | 100 | 27 g |

| Random Vibration Test Levels (120 s Duration) | | | |
|---|---|---|---|
| x and y values | | z values | |
| Frequency (Hz) | Target | Frequency (Hz) | Target |
| 20 | Ramp up with +6 dB/octave | 20 | Ramp up with +6 dB/octave |
| 80 | 0.13 $g^2$/Hz | 100 | 0.5 $g^2$/Hz |
| 400 | 0.13 $g^2$/Hz | 150 | 0.5 $g^2$/Hz |
| 2000 | Ramp down with −7 dB/octave | 200 | Ramp down to 0.08 $g^2$/Hz |
| Total | 8.9 g RMS | 700 | 0.08 $g^2$/Hz |
| | | 2000 | Ramp down with −7 dB/octave |
| | | Total | 11.1 g RMS |

| Shock Test Levels | | | |
|---|---|---|---|
| x and y values | | z values | |
| Frequency (Hz) | Target, SRS[a] ($Q = 10$) | Frequency (Hz) | Target, SRS ($Q = 10$) |
| 70 | 5 g | 70 | 5 g |
| 1000 | 200 g | 1000 | 50 g |
| 10,000 | 200 g | 10,000 | 50 g |

[a]SRS, shock response spectrum.

The program of environmental testing raised the fiber couplers to technology readiness level (TRL) 8, and the successful launch and operation of LISA Pathfinder will result in TRL 9 status based on ISO standard 16290 "Space Systems—Definition of the Technology Readiness Levels."

## 5. CONCLUSIONS

The design and testing of a spaceflight-qualified fiber coupler with excellent beam quality and beam pointing stability has been presented. Data from an implementation of the design that was used for the LISA Pathfinder optical bench interferometer, where two fiber couplers were used, demonstrates tailoring of beam expansion parameters during design and construction. This allows for optimization of the interference of combined beams from two individual fiber couplers.

**Funding.** Science and Technology Facilities Council (STFC) (ST/I00617X/1, ST/H000356/1); United Kingdom Space Agency (UKSA); University of Glasgow; Scottish Universities Physics Alliance (SUPA); Particle Physics and Astronomy Research Council (PPARC) (PP/D507258/1).

**Acknowledgment.** We wish to acknowledge support from the University of Glasgow and the Scottish Universities Physics Alliance (SUPA).

## REFERENCES

1. F. Antonucci, M. Armano, H. Audley, G. Auger, M. Benedetti, P. Binetruy, C. Boatella, J. Bogenstahl, D. Bortoluzzi, P. Bosetti, M. Caleno, A. Cavalleri, M. Cesa, M. Chmeissani, G. Ciani, A. Conchillo, G. Congedo, I. Cristofolini, M. Cruise, K. Danzmann, F. D. Marchi, M. Diaz-Aguilo, I. Diepholz, G. Dixon, R. Dolesi, N. Dunbar, J. Fauste, L. Ferraioli, D. Fertin, W. Fichter, E. Fitzsimons, M. Freschi, A. G. Marin, C. G. Marirrodriga, R. Gerndt, L. Gesa, F. Gilbert, D. Giardini, C. Grimani, A. Grynagier, B. Guillaume, F. Guzmán, I. Harrison, G. Heinzel, M. Hewitson, D. Hollington, J. Hough, D. Hoyland, M. Hueller, J. Huesler, O. Jeannin, O. Jennrich, P. Jetzer, B. Johlander, C. Killow, X. Llamas, I. Lloro, A. Lobo, R. Maarschalkerweerd, S. Madden, D. Mance, I. Mateos, P. W. McNamara, J. Mendes, E. Mitchell, A. Monsky, D. Nicolini, D. Nicolodi, M. Nofrarias, F. Pedersen, M. Perreur-Lloyd, A. Perreca, E. Plagnol, P. Prat, G. D. Racca, B. Rais, J. Ramos-Castro, J. Reiche, J. A. R. Perez, D. Robertson, H. Rozemeijer, J. Sanjuan, A. Schleicher, M. Schulte, D. Shaul, L. Stagnaro, S. Strandmoe, F. Steier, T. J. Sumner, A. Taylor, D. Texier, C. Trenkel, D. Tombolato, S. Vitale, G. Wanner, H. Ward, S. Waschke, P. Wass, W. J. Weber, and P. Zweifel, "LISA Pathfinder: mission and status," Class. Quantum Grav. **28**, 094001 (2011).
2. The LISA International Science Team, "LISA unveiling a hidden universe," LISA Assessment Study Report, ESA/SRE(2011)/3 (2011).
3. P. Amaro-Seoane, S. Aoudia, S. Babak, P. Binétruy, E. Berti, A. Bohé, C. Caprini, M. Colpi, N. J. Cornish, K. Danzmann, J.-F. Dufaux, J. Gair, O. Jennrich, P. Jetzer, A. Klein, R. N. Lang, A. Lobo, T. Littenberg, S. T. McWilliams, G. Nelemans, A. Petiteau, E. K. Porter, B. F. Schutz, A. Sesana, R. Stebbins, T. Sumner, M. Vallisneri, S. Vitale, M. Volonteri, and H. Ward, "Low-frequency gravitational-wave science with eLISA/NGO," Class. Quantum Grav. **29**, 124016 (2012).
4. P. A. Seoane, S. Aoudia, H. Audley, G. Auger, S. Babak, J. Baker, E. Barausse, S. Barke, M. Bassan, V. Beckmann, M. Benacquista, P. L. Bender, E. Berti, P. Binétruy, J. Bogenstahl, C. Bonvin, D. Bortoluzzi, N. C. Brause, J. Brossard, S. Buchman, I. Bykov, J. Camp, C. Caprini, A. Cavalleri, M. Cerdonio, G. Ciani, M. Colpi, G. Congedo, J. Conklin, N. Cornish, K. Danzmann, G. de Vine, D. DeBra, M. D. Freitag, L. D. Fiore, M. D. Aguilo, I. Diepholz, R. Dolesi, M. Dotti, G. F. Barranco, L. Ferraioli, V. Ferroni, N. Finetti, E. Fitzsimons, J. Gair, F. Galeazzi, A. Garcia, O. Gerberding, L. Gesa, D. Giardini, F. Gibert, C. Grimani, P. Groot, F. G. Cervantes, Z. Haiman, H. Halloin, G. Heinzel, M. Hewitson, C. Hogan, D. Holz, A. Hornstrup, D. Hoyland, C. Hoyle, M. Hueller, S. Hughes, P. Jetzer, V. Kalogera, N. Karnesis, M. Kilic, C. Killow, W. Klipstein, E. Kochkina, N. Korsakova, A. Krolak, S. Larson, M. Lieser, T. Littenberg, J. Livas, I. Lloro, D. Mance, P. Madau, P. Maghami, C. Mahrdt, T. Marsh, I. Mateos, L. Mayer, D. McClelland, K. McKenzie, S. McWilliams, S. Merkowitz, C. Miller, S. Mitryk, J. Moerschell, S. Mohanty, A. Monsky, G. Mueller, V. Müller, G. Nelemans, D. Nicolodi, S. Nissanke, M. Nofrarias, K. Numata, F. Ohme, M. Otto, M. Perreur-Lloyd, A. Petiteau, E. S. Phinney, E. Plagnol, S. Pollack, E. Porter, P. Prat, A. Preston, T. Prince, J. Reiche, D. Richstone, D. Robertson, E. M. Rossi, S. Rosswog, L. Rubbo, A. Ruiter, J. Sanjuan, B. Sathyaprakash, S. Schlamminger, B. Schutz, D. Schütze, A. Sesana, D. Shaddock, S. Shah, B. Sheard, C. F. Sopuerta, A. Spector, R. Spero, R. Stanga, R. Stebbins, G. Stede, F. Steier, T. Sumner, K.-X. Sun, A. Sutton, T. Tanaka, D. Tanner, I. Thorpe, M. Tröbs, M. Tinto, H.-B. Tu, M. Vallisneri, D. Vetrugno, S. Vitale, M. Volonteri, V. Wand, Y. Wang, G. Wanner, H. Ward, B. Ware, P. Wass, W. J. Weber, Y. Yu, N. Yunes, and P. Zweifel, "The gravitational universe," 2013, p.http://arxiv.org/abs/1305.5720.
5. D. I. Robertson, E. D. Fitzsimons, C. J. Killow, M. Perreur-Lloyd, H. Ward, J. Bryant, A. M. Cruise, G. Dixon, D. Hoyland, D. Smith, and J. Bogenstahl, "Construction and testing of the optical bench for LISA Pathfinder," Class. Quantum Grav. **30**, 085006 (2013).
6. D.-H. Gwo, "Ultra-precision and reliable bonding method," U.S. patent 6,284,085 B1 (4 September 2001).
7. A.-M. A. van Veggel and C. J. Killow, "Hydroxide catalysis bonding for astronomical instruments," Adv. Opt. Technol. **3**, 293–307 (2014).
8. C. J. Killow, E. D. Fitzsimons, J. Hough, M. Perreur-Lloyd, D. I. Robertson, S. Rowan, and H. Ward, "Construction of rugged, ultrastable optical assemblies with optical component alignment at the few microradian level," Appl. Opt. **52**, 177–181 (2013).
9. "Diamond SA datasheet BDD 1950099," 2014, http://www.diamond-fo.com/dms/site-diamond/documents/Products-and-Library/products/datasheets/AVIO_AVIM_e/AVIO%20AVIM%20datasheet.pdf.
10. E. D. Fitzsimons, J. Bogenstahl, J. Hough, C. J. Killow, M. Perreur-Lloyd, D. I. Robertson, and H. Ward, "Precision absolute positional measurement of laser beams," Appl. Opt. **52**, 2527–2530 (2013).
11. F. G. Cervantes, G. Heinzel, A. F. G. Marín, V. Wand, F. Steier, O. Jennrich, and K. Danzmann, "Real-time phase-front detector for heterodyne interferometers," Appl. Opt. **46**, 4541–4548 (2007).
12. A. E. Siegman, *Lasers* (Oxford University, 1981).